RSC Mechanochemistry

ROYAL SOCIETY OF CHEMISTRY

PAPER

View Article Online
View Journal | View Issue

Cite this: *RSC Mechanochem.*, 2025, **2**, 91

Rapid mechanochemical synthesis and properties in Pb–Bi–S system†‡

Peter Baláž, [a] Erika Dutková, *[a] Nina Daneu,[b] Michal Hegedüs,[c] Matej Baláž, [a] Emmanuel Guilmeau, [d] Róbert Džunda,[e] Mária Bali-Hudáková, [a] Veronika Garbárová,[a] Jianzhong Jiang[f] and Marcela Achimovičová [a]

We prepared a ternary sulfide with a stoichiometry close to $Pb_6Bi_2S_9$ from PbS, Bi, and S precursors using mechanochemical synthesis. After 5 min of high-energy milling, conversion of the precursors to $Pb_{5.95}Bi_{2.02}S_{9.03}$ was confirmed using scanning electron microscopy (SEM) and energy dispersive X-ray spectroscopy (EDXS). Further milling (up to 120 min) led to the metal-enriched and sulfur-deficient composition $Pb_{6.40}Bi_{2.24}S_{8.36}$. Values of the specific surface area of the produced powder samples were used as an indicator of the transition from the mechanical activation mode to the mechanochemical synthesis mode. The products crystallized in the galena structure, with the crystallite size ranging from 5 to 15 nm, as determined by X-ray diffractometry (XRD) with Rietveld refinement and transmission electron microscopy (TEM). The dissolution of Bi from the synthesized nanocrystals corresponds to changes in the specific surface area. Spark plasma sintering (SPS) densified ingots in the temperature range of 300–525 K exhibit semiconducting properties and a low thermal conductivity of 0.38–0.5 W m^{-1} K^{-1}, making them promising for thermoelectric applications. The possibility of modifying the properties of a ternary Pb–Bi–S system by mechanochemistry paves the way for the synthesis of more sophisticated ternary and multinary structures suitable for energy applications.

Received 23rd September 2024
Accepted 31st October 2024

DOI: 10.1039/d4mr00107a

rsc.li/RSCMechanochem

1. Introduction

Several new prospective energy materials in sulfide thermoelectrics have emerged recently. The incorporation of new elements into binary sulfides is a suitable option for modifying their thermoelectric behaviour. Lead sulfide (galena) PbS represents a good example. Its chemical modification using Na and Cl has led to changes from a p-type to a n-type semiconductor, consequently changing its thermoelectric behaviour.[1] Similarly, wet processing of PbS with Ag also had a positive impact.[2] The high willingness of the PbS matrix to accept foreign elements has also been observed in nature. An excess of Ag and Bi with their high solid solubility represents the common incidence of these elements in lead ores.[3] In particular, Bi forms a great variety of compounds. Several compositions have been identified, *e.g.* $Pb_{0.816}Bi_{0.123}S$ (lead bismuth sulfide), $Pb_{0.89}Bi_{0.22}S_{1.22}$ (galena Bi-bearing, syn), $Pb_{3.82}Bi_{0.94}S_{5.24}$ (bismuth lead sulfide), $Pb_{5.48}Bi_{2.34}S_9$ (heyrovskýite, syn) and $Pb_{5.92}Bi_{2.08}S_9$ (aschamalmite). A variety of further compositions exists, such as cosalite $Pb_2Bi_2S_5$, lilianite $Pb_3Bi_2S_6$, galenobismutite $PbBi_2S_4$,[4] cannizzarite $Pb_4Bi_6S_{13}$ [3] and xilingolite $Pb_{3.18}Bi_{1.81}S_6$.[5] Some of these structures are susceptible to the impact of mechanical energy, as has been documented for $Pb_6Bi_2S_9$ in pressure-induced phase transitions.[4,6,7]

In terms of composition, all the mentioned varieties represent a challenge for studying the incorporation of Bi into PbS in a synthetic manner. The application of high-energy milling for such studies is an extremely effective tool as demonstrated recently for various solids.[8–14] In particular, ternary sulfides, as analogues to the Pb–Bi–S system, were recently thoroughly studied.[15–19]

[a]*Institute of Geotechnics Slovak Academy of Sciences, 04001 Košice, Slovakia. E-mail: balaz@saske.sk; dutkova@saske.sk; balazm@saske.sk; krulakova@saske.sk; garbarova@saske.sk; achimovic@saske.sk; Tel: +421-55-792-2606*

[b]*Advanced Materials Department, Jozef Stefan Institute, S1-1000 Ljubljana, Slovenia. E-mail: nina.daneu@ijs.si*

[c]*Synthon s.r.o., 67801 Blansko, Czech Republic. E-mail: michal.hegedus@gmail.com*

[d]*CRISMAT, CNRS, Normandie University, ENSICAEN, UNICAEN, 6, 14000, France. E-mail: emmanuel.guilmeau@ensicaen.fr*

[e]*Institute of Materials Research, Slovak Academy of Sciences, 04001 Košice, Slovakia. E-mail: rdzunda@saske.sk*

[f]*Fuyao University of Science and Technology, Fuzhou, 350109, Fujian Province, P. R. China. E-mail: jiangjz@zju.edu.cn*

† The paper is devoted to the memory of Czechoslovak Nobel Prize laureate Jaroslav Heyrovský after whom the natural mineral heyrovskýite $Pb_6Bi_2S_9$ was named.

‡ Electronic supplementary information (ESI) available. See DOI: https://doi.org/10.1039/d4mr00107a

Based on this knowledge, the aim of this paper was to elucidate the structure and properties of a new mechanochemically formed Pb–Bi–S system.

2. Results and discussion

2.1. Mechanochemical synthesis and structural characterization of Pb–Bi–S system

The XRD patterns of the milled powder samples are given in Fig. 1a and S2.‡ The phase transformation in the Pb–Bi–S system is documented by the powder diffraction patterns obtained during mechanochemical treatment for milling time, t_M = 0.5–120 min.

At the beginning of milling (t_M = 0.5–1 min), only non-consumed bismuth (ICDD PDF 01-085-1329) and PbS galena (ICDD PDF 00-005-0592) can be identified in the system. In this case, the high-energy milling causes only homogenization and mechanical activation. After 5 min, elemental bismuth cannot be detected anymore. Diffraction peaks become broader as the crystallite size is reduced significantly. In contrast, no binary phase Bi–S system (such as bismuthinite Bi_2S_3) can be identified in the diffraction patterns.

The fact that Bi is clearly incorporated into the ternary structure of PbS can also be clearly seen from Fig. S3.‡ The mechanical activation of pure Bi for 5 min leads only to partial weak amorphization, but all of its diffraction peaks are clearly

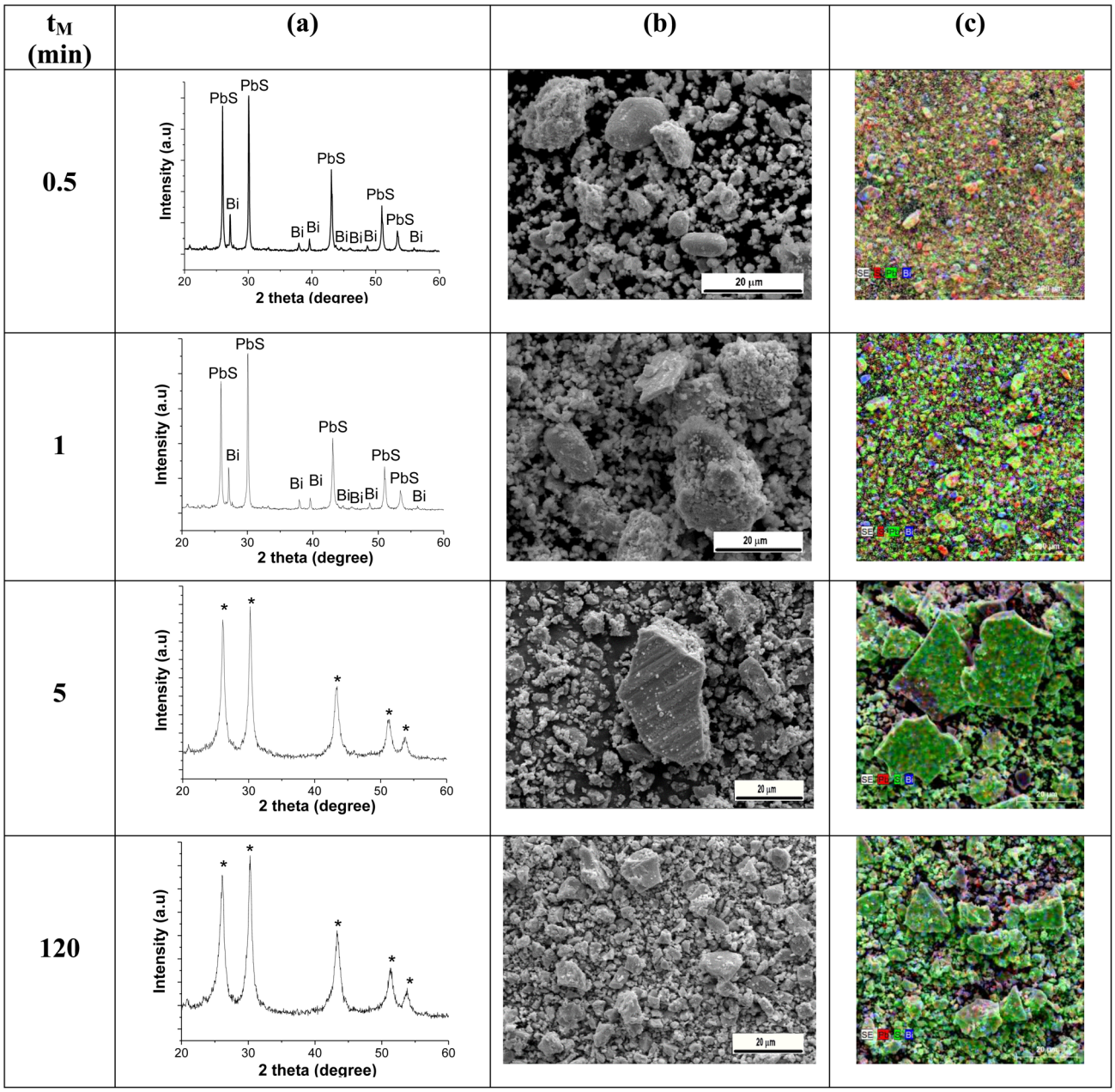

Fig. 1 (a) XRD patterns (stars correspond to PbS enriched with Bi in a new Pb–Bi–S system), (b) SEM images, (c) elemental mapping after mechanochemical synthesis for selected milling times: Pb – red, S – green, Bi – blue.

visible (Fig. S3c‡), unlike the mixture of PbS + Bi, where no Bi can be seen (Fig. S3a‡). The mechanical activation of pure PbS also leads to its partial amorphization; however, this occurs to a significantly lower extent than in the case of the PbS + Bi mixture (Fig. S3b‡). This can be confirmed by properly checking the intensity of the peaks of the PbS and PbS + Bi samples. A much higher intensity can be seen in the case of pure PbS, indicating that the structure is much more resistant to the effect of milling than that of the PbS + Bi system; as in the latter case, the background noise is much higher. It should be noted that all the measurements were performed under the same conditions. In general, these results provide definite proof of the incorporation of Bi into the PbS structure.

This suggests that Bi metal has already been incorporated into the galena lattice after a very short milling time. All the XRD patterns obtained after milling for 5–120 min are practically identical and contain only galena reflections, with a small amount of $PbSO_4$ stemming partly from the initial precursor and partly from oxidation (Fig. S2‡). The particles of $PbSO_4$ initially introduced together with the PbS precursor might serve as crystallization cores, around which the formation of this compound might take place.

The SEM analyses (Fig. 1b) confirmed that all the samples are composed of agglomerated particles. The sample milled for 0.5 min is composed mainly of agglomerates of several micrometers in diameter, with individual particles of different distributions and morphologies. In samples milled for 1 min, rounded Bi particles are visible next to the formed agglomerates. With increasing milling time (5 min), rounded Bi particles are not observed anymore, and the product is composed of large flat agglomerated particles surrounded by smaller ones. These flattened particles are a result of plastic deformation of solids, which frequently follows the agglomeration step.[20] The flat particles are dense, practically without porosity. Finally, after 120 min of mechanochemical synthesis, the average size of the agglomerates becomes smaller, with a more uniform size distribution.

The distribution of elements (Pb, Bi and S) at the microscale was investigated using SEM/EDX analyses, and the results are presented in Table 1. The results are in accordance with the XRD patterns (Fig. 1a and S2‡). After 5 min of milling, a composition close to the initial stoichiometry was obtained ($Pb_{5.95}Bi_{2.02}S_{9.03}$; Pb : Bi = 2.95), whereas sulfur-deficient powders with a similar Pb : Bi ratio are observed after 120 min of milling ($Pb_{6.40}Bi_{2.24}S_{8.36}$; Pb : Bi = 2.86). The deficiency in sulfur is most likely due to evaporation from the reaction system during milling. The constant Pb : Bi ratio of around 2.9 in both samples supports this interpretation. Generally, sulfur bonds are the most amenable parts in ternary sulfides, as demonstrated in several (Cu–Fe–S) systems.[21]

The crystallite sizes of 15 and 10 nm in the samples milled for 5 and 120 min were initially determined from XRD by Rietveld refinement (Table S1‡). Elemental mapping for samples milled for t_M = 5 min and 120 min was performed. From the EDX elemental mapping images (Fig. S4‡), all the elements are uniformly distributed in both samples, suggesting the homogeneous nature of the Pb–Bi–S system at the microscale. None of the elements show a tendency for the agglomeration and segregation of certain elements.

Further, the samples were investigated using TEM with SAED and EDX. The low-magnification TEM image taken at the edge of an agglomerated particle after 5 min of milling is shown in Fig. 2. The sample is composed of agglomerated randomly oriented nanocrystallites with an estimated size in the 10 nm range. The nanocrystallites are separated with many grain boundaries. They can effectively suppress lattice thermal conductivity, which is a crucial factor in thermoelectrics.[22]

The fast Fourier transformation (FFT) pattern yields diffraction rings with d-values characteristic for galena. Magnified atomic-resolution images of the sample from thin electron transparent regions of the sample (areas 1–4 in Fig. 2a) additionally confirm that the crystallites have the galena structure (Fig. 2b).

Quantitative maps of agglomerated particles after 5 min of milling show that the distribution of all elements in the powders is fairly homogenous at the nanoscale, although some small local variations were detected in the Pb : Bi ratio (Fig. 2c). The results imply that Bi and Pb are randomly incorporated into the structure of the ternary sulfide with the overall galena structure and approximate stoichiometry of $Pb_6Bi_2S_9$. Phases with this stoichiometry and a more complex crystal structure, such as aschamalmite (Fig. 2d), were not found in this sample. Similar characteristics were also obtained for the sample after 120 min of milling.

2.2. Surface properties and chemical reactivity

The evolution of the surface area, S_{BET}, in the Pb–Bi–S system as a function of milling time, t_M, is depicted in Fig. 3a. The sharp increase in S_{BET} at t_M = 0.5–3 min (log t_M = 1.48–2.26) corresponds to comminution of reacting elements. As mentioned earlier, in this region, only homogenization and mechanical activation play the dominant role. Later, as the surface area diminishes, agglomerates are formed, which serve as pre-deposition sites for mechanochemical synthesis. Intimate contact between Bi and PbS is needed to produce the product in the Pb–Bi–S system. This phenomenon is an inevitable premise for the occurrence of solid-state diffusion of Bi into the PbS structure to form $Pb_xBi_yS_z$ compounds.

Based on S_{BET} data, a mechanochemical equilibrium comes into existence after 5 min.[23] During the phenomenon, the amount of new particles formed is in equilibrium with the number of particles that are agglomerated and forming larger entities.[24]

During the entire interval of milling, the course of Bi dissolution, c_{Bi}, as well as surface area, S_{BET}, is shown in Fig. 3a and b (c_{Bi} corresponds to the concentration of Bi in the leached solution). For milling times longer than 5 min, the plots are similar and the dependence on milling time, t_M, can be described using exponential empirical equations (see ESI‡) with very close and statistically satisfactory coefficients of determination, R^2. From these equations, the rate constants, k_{BET} and k_{Bi}, were calculated. Their similarity demonstrates a close relation between Bi and S_{BET} behaviour. Bismuth dissolution from the Pb–Bi–S structure needs disruption of its bonds with Pb and S and therefore reflects the

Table 1 SEM and EDX analyses of the Pb–Bi–S system

Point no.	Milling time (min)	Atomic% Pb	Bi	S	Composition	SEM
1		35.3	12.1	52.6		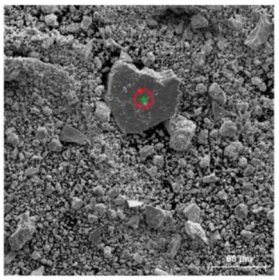
2		35.5	12.1	52.4		
3		34.5	11.2	54.3		
4		34.5	12.1	52.4		
						Point No. 1
5	5	34.7	12.2	53.2	$Pb_{5.95}Bi_{2.02}S_{9.03}$	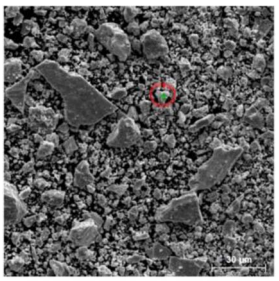
6		34.9	11.9	53.1		
7		34.5	12.0	53.5		
8		36.1	12.0	52.4		
						Point No. 8
Mean $\mu \pm \sigma$		**35.0**	**11.9**	**53**		
Standard deviation σ		**±0.6**	**±0.3**	**±0.7**		
9		38.4	14.6	47.0		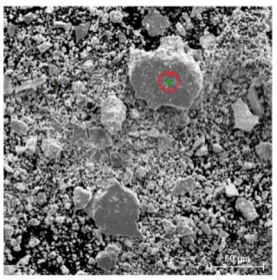
10		37.0	12.6	50.4		
11		38.6	13.4	48.0		
12		39.3	14.8	45.9		
13		38.0	12.8	49.2		
						Point No. 9
14	120	36.5	12.7	50.9	$Pb_{6.40}Bi_{2.24}S_{8.36}$	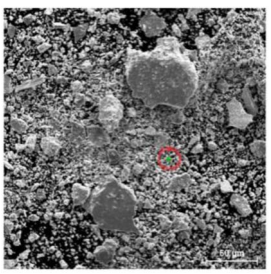
15		38.3	13.3	48.4		
16		38.2	13.1	48.7		
17		36.9	13.1	50.0		
18		36.7	12.8	50.5		
19		36.2	12.0	51.9		
						Point No. 14
Mean $\mu \pm \sigma$		**37.6**	**13.2**	**49.2**		
Standard deviation σ		**±1**	**±0.8**	**±1.7**		

bulk behaviour of the studied system. In contrast, the dissolution of Bi starts at the surface of the Pb–Bi–S structure and therefore the surface represented by S_{BET} values also intervenes. As a consequence, the similarity between S_{BET} and c_{Bi} plot in dependence on the milling time, t_M, is proof of the structural sensitivity of the Pb–Bi–S system.

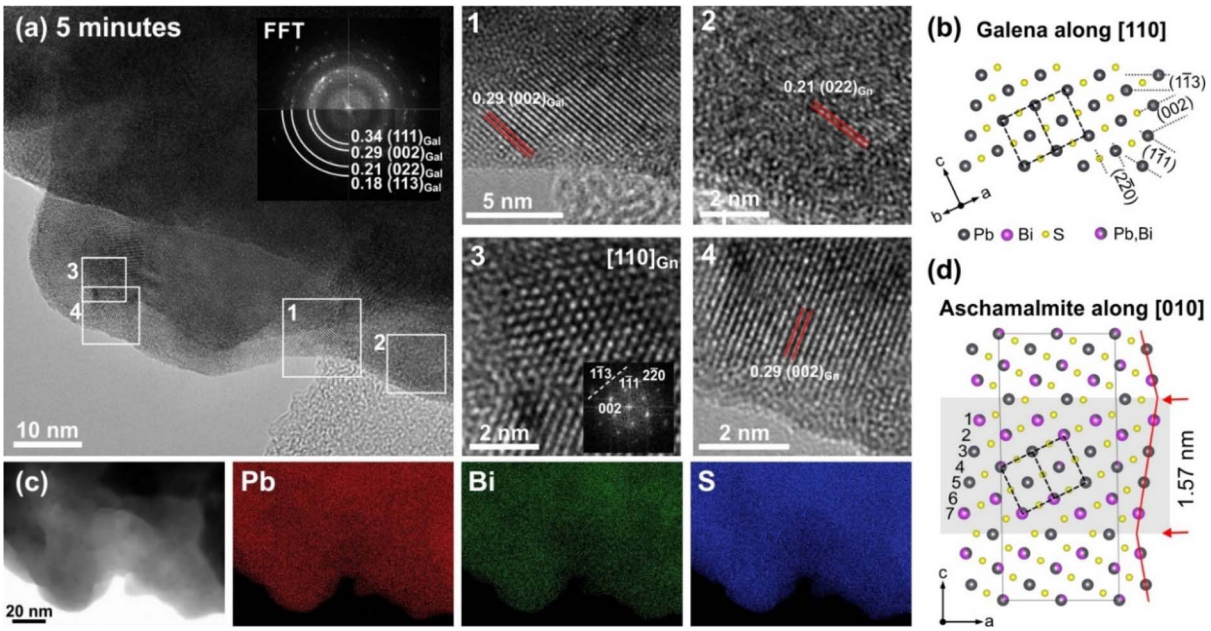

Fig. 2 (a) TEM micrograph of the sample after 5 min of milling; (Insert): FFT patterns composed of diffraction rings that belong to galena. Areas 1–4 show magnified nanocrystallites with different edge-on oriented lattice planes typical for galena. (b) Crystal structure of galena oriented along the [110] zone axis. (c) EDX maps of Pb, Bi and S reveal homogenous distribution of elements at the nanoscale. (d) Crystal structure of aschamalmite oriented along the [010] zone axis where common structural elements with galena can be observed.

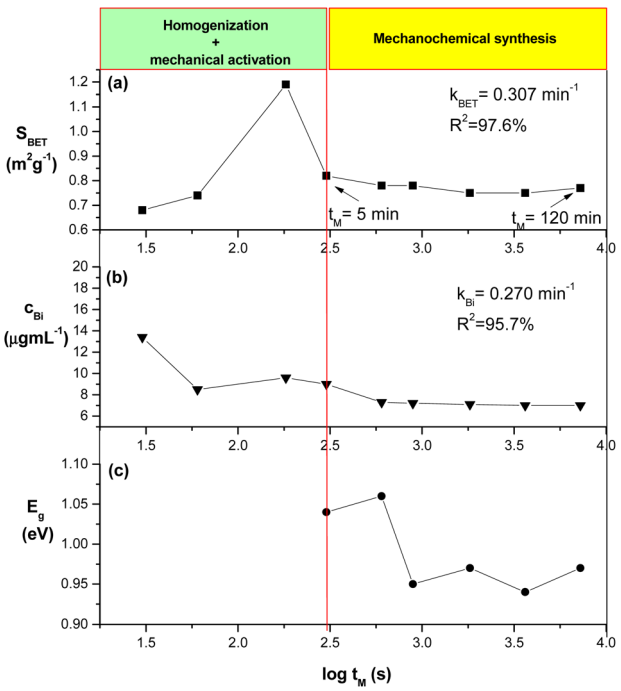

Fig. 3 Specific surface area, S_{BET} (a), Bi leachability, c_{Bi} (b) and band gap, E_g (c) *vs.* milling time, t_M (in logarithm scale) in the Pb–Bi–S system.

2.3. Band gap sensitivity

The value of the band gap, E_g, which characterizes the difference between the valence and conduction bands in semiconductors, represents a crucial parameter for determining their properties. Broadening or narrowing of E_g reflects structural and microstructural changes. Several external interventions can be applied for band gap tuning.

The influence of pressure, temperature and doping for different semiconductors has been described in the literature.[25–27]

Recently, the tunability of E_g in a high-energy milled chalcopyrite $CuFeS_2$ was evidenced for the first time, and the structural sensitivity of E_g was documented.[28] The influence of the agglomeration of chalcopyrite particles on the value of E_g was proved.

For the Pb–Bi–S system, the dependence of band gap, E_g, on the milling time, t_M, is shown in Fig. 3c. In comparison with Fig. 3a and b, the values of E_g are also stabilized by higher milling times. We speculate that all these common phenomena are the consequence of changes in the solid-state properties of the Pb–Bi–S system. Its further destabilization would be only possible by a higher supply of mechanical energy, *e.g.*, a longer milling time and/or by the application of non-equilibrium approaches, such as spark plasma sintering (SPS).

2.4. Characterization of the sample after SPS

To check the potential of the prepared materials for thermoelectric applications, the milled powders were densified using spark plasma sintering (SPS). XRD patterns of the SPS densified powders after milling for 5 and 120 min are provided in the ESI (Fig. S5).‡ The obtained XRD patterns are very similar to those before SPS (Fig. 1a), indicating that the powders remained stable during sintering. The sample after 120 min of milling was inspected using TEM (Fig. 4). The analysis revealed that the

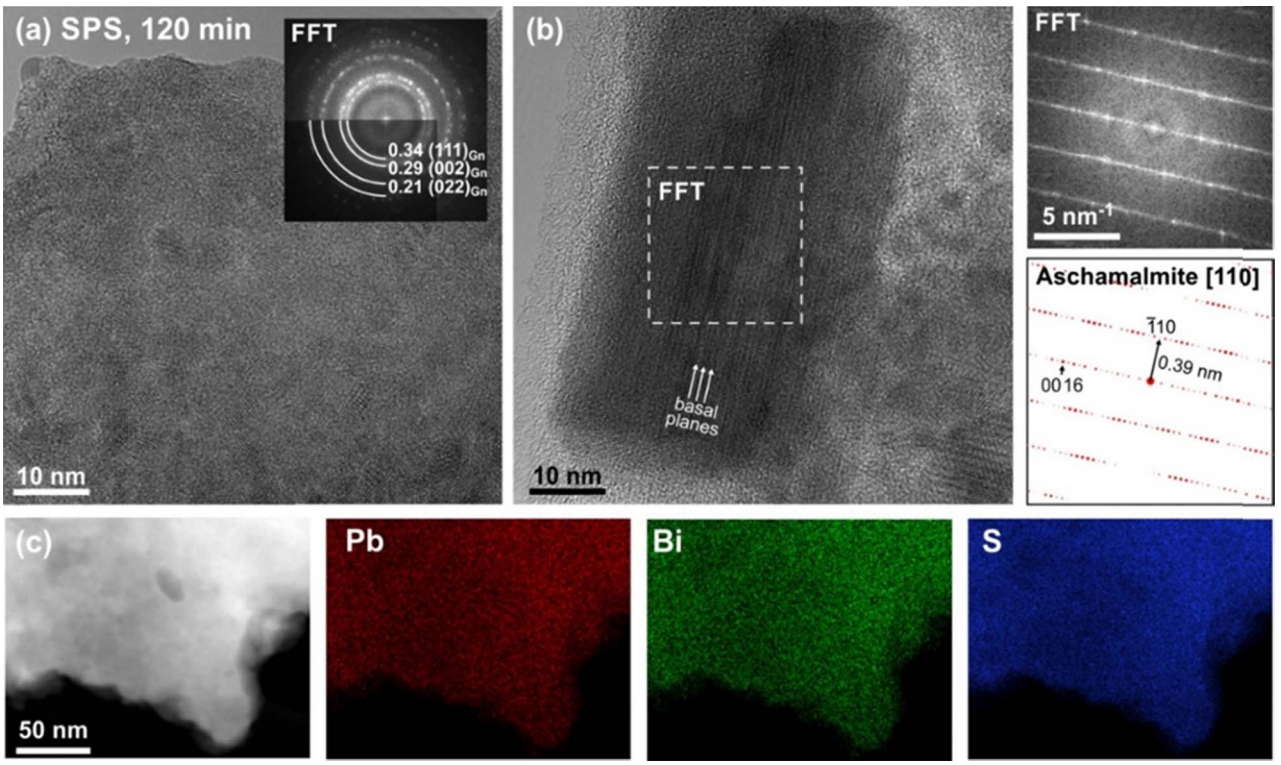

Fig. 4 (a) High-resolution TEM image of the 120 milled sample after SPS. The sample is composed of tightly bonded nanocrystallites, and the diffraction rings in the FFT pattern can be indexed with galena. (b) Few larger grains with structural characteristics of aschamalmite were found in the sample. (c) The EDX mapping shows a homogenous distribution of Pb, Bi and S in the sample at the nanoscale.

majority of the sample is composed of nanosized crystallites with a galena structure according to the fast Fourier transformation (FFT) pattern.

By careful inspection, few larger grains with distinctly different crystal structure were identified in this sample. One such larger grain measuring approximately 35 × 60 nm in cross section is shown in Fig. 4b. The grain is intersected by many lattice planes running parallel to the longer axis. The experimental FFT pattern was calculated from the rectangular region marked on the grain. The FFT pattern is composed of lines of continuous reflections with spacing of around 0.39 nm and it can be fitted with a simulated FFT pattern of aschamalmite oriented along the [110] zone axis (lower right). The experimental pattern is composed of streaks instead of dots (as observed in the simulated FFT pattern) due to the imperfect tilt of the grain and/or irregular periodicity in the direction of the *c*-axis. Aschamalmite and galena are structurally similar, as shown in Fig. 2. In comparison to cubic galena, aschamalmite ($Pb_{6-3x}Bi_{2+x}S_9$, space group $C2/m$) belongs to the lillianite homologous series, where the members are based on pseudo-mirror-related PbS-like slabs of various thicknesses (PbS archetype) along the *c*-axis.[29] In aschamalmite, the number of atomic layers (113 layers of galena) in one slab is 7 (heyrovskýite homeotypic series, ^{7}L) and Pb cations occupying selected structural sites are partially replaced by Bi. More details about the structure of aschamalmite are given in paper Callegari and Boiocchi.[29] It seems that at lower temperatures (high-energy milling), Bi simply replaces Pb in the galena structure, whereas recrystallization to aschamalmite occurs at higher temperatures, as generated during SPS treatment. It is likely that longer sintering times would yield more aschamalmite. The existence of the aschamalmite phase can also be supported by a screenshot generated from the XRD analysis program, showing the highest match of this phase (Fig. S6‡). The diffractogram was taken for the sample milled for 120 min and treated with SPS. However, to verify these experimental findings, Crystal Maker program was performed (Fig. S7‡) for the nanocrystalline sample (15 nm). The simulation shows that it is almost impossible to distinguish between the galena and aschamalmite phases using powder XRD if the crystalline size is so small.

2.5. Thermoelectric properties

Fig. 5 shows the electrical properties in the sintered samples prepared using $t_M = 5$ and 120 min over the temperature range of 300–525 K. Both samples exhibit a decrease in the electrical resistivity (ρ) and the absolute value of the Seebeck coefficient (S) with the increase in temperature, indicating intrinsic semiconducting behaviour. The values of the Seebeck coefficients are higher than those reported by Maji *et al.*[30] and Liu *et al.*[31] in $PbBi_2S_4$. The values of the thermal conductivity range between 0.38 and 0.5 W m^{-1} K^{-1} in the measured temperature range. These values are lower than those reported in $PbBi_2S_4$ and $Pb_3Bi_2S_6$.[30,32,33]

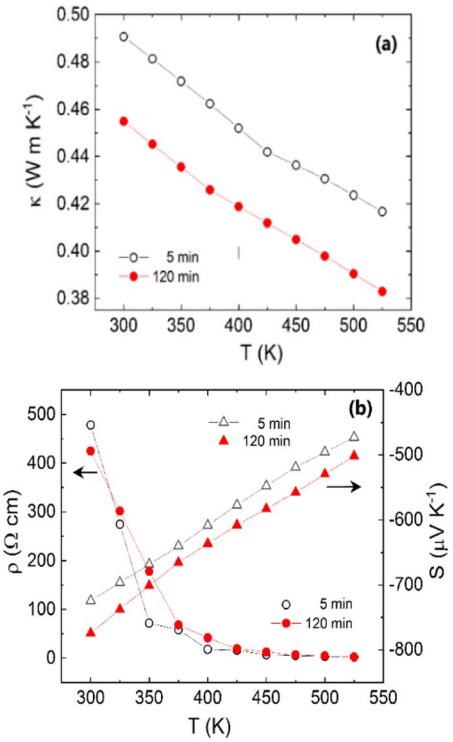

Fig. 5 Thermal conductivity, κ (a), resistivity, ρ and Seebeck coefficient, S (b) *vs.* temperature, T for milling time, $t_M = 5$ min and 120 min, respectively.

This difference can be explained by the smaller particle size and lower geometrical density in the present case. Chemical inhomogeneities at the lattice scale in combination with abundant grain boundaries due to the nanosized crystallites can effectively suppress lattice thermal conductivities and are thus ideal for the preparation of thermoelectric materials with high efficiency.[22]

3. Materials and methods

3.1. Materials

For mechanochemical synthesis in the Pb–Bi–S system, a combination of compounds and elements has been applied. Galena, syn PbS (Sigma-Aldrich, USA), bismuth, syn Bi (Sigma-Aldrich, Taufkirchen, Germany) and sulfur, syn S (Sigma-Aldrich, USA) were used as precursors. XRD patterns of the starting precursors are given in Fig. S1.‡ All diffractograms correspond well to the reference cards of the given compounds provided by the International Centre for Diffraction Data (ICDD). Traces of anglesite $PbSO_4$ were detected in the starting PbS.

3.2. Methods

3.2.1. Mechanochemical synthesis. Mechanochemical synthesis was performed in a laboratory planetary Pulverisette 6 ball mill (Fritsch, Germany) working under the following conditions: a 250 mL tungsten carbide milling chamber, tungsten carbide milling balls with a diameter of 10 mm and a total mass of 360 g, revolutions of the mill at 500 min^{-1}, a milling time of 0.5–120 min, an argon atmosphere and a ball-to-powder ratio 72 : 1. In a typical experiment with 5 g mass input into the milling chamber, the following amounts of reaction precursors were applied: 3.682 g of PbS, 1.072 g of Bi and 0.246 g of S. Each 30 min of milling was followed by a 30 min break (cooling break).

3.2.2. Spark plasma sintering (SPS). The mechanochemically treated powders were introduced into graphite dies that had a diameter of 10 mm and were consolidated using spark plasma sintering (SPS-FCT HPD 25, Germany) at a temperature of 573 K for a duration of 30 min, under a pressure of 64 MPa. The heating and cooling rates were set at 50 K min^{-1} and 20 K min^{-1}, respectively. The resulting pellets had a diameter of 10 mm and a thickness of around 9 mm, exhibiting geometrical densities of around 90% of the theoretical value.

3.3. Characterization techniques

3.3.1. X-ray diffractometry (XRD). For the determination of phase composition in the Pb–Bi–S system, the XRD patterns were collected. A D8 Advance diffractometer (Bruker, Germany) with CuK_α radiation in the Bragg–Brentano configuration or a Panalytical Empyrean diffractometer with the same geometry was used for this purpose. The generator was set up at 40 kV and 40 mA in both cases. The divergence and receiving slits were 0.3° and 0.1 mm, respectively. The XRD patterns were recorded in the range of $2\theta = 20$–65° with a step size of 0.05° and $2\theta = 4$–90° with a step size of 0.01° when using Bruker and Panalytical diffractometers, respectively. The XRD line broadening was analysed by refining regular Thompson–Cox–Hastings pseudo-Voigt function parameters. In order to obtain a suitable geometric set-up and to eliminate instrumental broadening, the instrumental resolution function was determined by refining a LaB_6 standard specimen. The ICDD PDF database for phase identification was utilized.

3.3.2. Scanning electron microscopy (SEM) and elemental analysis (EDX). The morphology and size of the powder particles were investigated using a Tescan Vega 3 LMU scanning electron microscope (SEM) (Tescan, Czech Republic) with an accelerating voltage of 20 kV. In order for the samples to be conductive, the powder was covered by a layer of gold using a Fine Coat Ion Sputter JFC 1100. To obtain information about the chemical composition of the particles, a Tescan Bruker XFlash Detector 410 M energy dispersive X-ray spectrometer (EDX) (Bruker, Germany) was used.

3.3.3. Transmission electron microscopy (TEM) and elemental analysis (EDX). Transmission electron microscopy (TEM) analyses were performed on a Spectra 300 (Thermo Fisher) microscope operated at 200 kV. The microscope was equipped with a Ceta M/S 4k camera for high-resolution imaging and a Super-X EDX detector for elemental mapping. For TEM analyses, a small amount of the sample was ultrasonically homogenized in absolute alcohol for 5 min. Further, a droplet of the suspension was applied onto a lacey carbon-coated Ni grid and dried. Prior to the TEM analyses, the

samples were carbon-coated to prevent charging under the electron beam.

3.3.4. Specific surface area measurement (S_{BET}). The S_{BET} measurements were performed on a Gemini 2360 sorption apparatus (Micromeritics, USA) using the low-temperature nitrogen adsorption method.

3.3.5. UV-vis spectroscopy. Absorption spectra were measured using a Helios Gamma (Thermo Electron Corporation, UK) UV-vis spectrophotometer in the range of 200–800 nm in a quartz cell. The samples were dispersed in absolute ethanol by ultrasonic stirring. The direct optical band gap energy, E_g was determined using the Tauc equation

$$(\alpha h\nu)^2 = A(h\nu - E_g) \quad (1)$$

where α is the absorption coefficient, A is a constant, h is Planck's constant, and ν is frequency. E_g was estimated by plotting $(\alpha h\nu)^2$ as a function of the photon energy $h\nu$. Extrapolating the straight-line portion of the Tauc plot for a zero absorption coefficient ($\alpha = 0$) gives the optical band gap energy.

3.3.6. Chemical reactivity (dissolution tests). To evaluate the bonding of bismuth in the synthesized Pb–Bi–S system and/or determine the presence of free (non-bound) Bi, dissolution tests were performed. Sodium thiosulfate $Na_2S_2O_3$ solution was used for dissolution. In this lixiviant, Bi sulfides form soluble thiosulfate complexes.[34] The dissolution conditions were as follows: 250 mL solution of 100 g L^{-1} $Na_2S_2O_3$, weight of sample 500 mg, dissolution time 30 min and dissolution temperature 30 °C. The concentration of Bi was determined by the method of atomic absorption spectroscopy using a SPECTRAA L40/FS atomic absorption spectrometer (Varian, Crawley, UK).

3.3.7. Thermoelectric properties. The present study reports on the concurrent measurement of electrical resistivity (ρ) and Seebeck coefficient (S) from sintered ingots of dimensions 3 × 3 × 9 mm^3. The measurements were carried out using a ULVAC-ZEM3 instrument under partial helium pressure over a temperature range of 300 K to 525 K. The thermal diffusivity was measured on a 6 × 6 mm^2 sample using a NETZSCH LFA-457 apparatus subjected to an argon flow. The thermal conductivity (κ) was calculated by multiplying its geometrical density, thermal diffusivity, and theoretical heat capacity, as per the Dulong–Petit approximation.

4. Conclusions

In this work, a mixture of precursors (PbS, Bi, S) has been treated by high-energy milling. After short period of mechanical activation (0.5–3 min), the incorporation of Bi into the disordered PbS structure is observed. The absence of elemental Bi in the reaction mixture is confirmed after 5 min. Using more drastic treatment (longer milling time, high temperature by spark plasma sintering), the synthetic aschamalmite $Pb_6Bi_2S_9$ is detected in recrystallized grains. The treated Pb–Bi–S system proceeds from mechanical activation mode to the mechanochemical synthesis mode. The whole event takes place in a nanocrystalline space, where the size of the crystallites is in the range 5–15 nm. The whole spectrum of characterization techniques was applied, such as XRD, SEM, HRTEM, EDX, specific surface area measurement, UV-vis and dissolution tests. The products were treated with SPS to obtain densified pellets for investigating thermoelectric performance. The ability of phase deformation together with the rigid PbS structure and the possibility of Bi incorporation into its lattice was one of the key topics of this paper. Chemical inhomogeneities at the lattice scale, along with abundant grain boundaries due to nanosized crystallites, suppress lattice thermal conductivities and are thus ideal for high-efficiency thermoelectric materials. Nowadays, mechanochemical synthesis is also well accepted for the preparation of verified thermoelectric materials such as PbTe as a representative of well-proved chalcogenide thermoelectrics.[35]

Data availability

The datasets generated during and/or analysed during the current study are available from the corresponding author on reasonable request.

Author contributions

Conceptualization: Peter Baláž. Funding acquisition: Matej Baláž. Investigation: Erika Dutková, Emmanuel Guilmeau, Matej Baláž, Michal Hegedus, Nina Daneu, Róbert Džunda, Veronika Garbárová, Jianzhong Jiang, Marcela Achimovičová. Methodology: Erika Dutková, Emmanuel Guilmeau, Matej Baláž, Michal Hegedus, Nina Daneu, Róbert Džunda, Mária Bali-Hudáková. Project administration: Peter Baláž. Resources: Matej Baláž. Supervision: Peter Baláž. Validation: Peter Baláž. Visualization: Erika Dutková, Emmanuel Guilmeau, Nina Daneu, Róbert Džunda. Writing – original draft: Peter Baláž. Writing – review & editing: Erika Dutková, Emmanuel Guilmeau, Matej Baláž, Michal Hegedus, Nina Daneu, Róbert Džunda, Mária Bali-Hudáková, Jianzhong Jiang, Marcela Achimovičová.

Conflicts of interest

The authors declare no conflict of interest.

Acknowledgements

This work was supported by the Slovak Grant Agency VEGA (project 2/0112/22 and 2/0036/23).

References

1 L. D. Zhao, J. Q. He, S. Q. Hao, C. I. Wu, T. P. Hogan, C. Wolverton, V. P. Dravid and M. G. Kanatzidis, *J. Am. Chem. Soc.*, 2012, **134**, 16327–16336.
2 M. Ibáñez, Z. S. Luo, A. Genç, L. Piveteau, S. Ortega, D. Cadavid, O. Dobrozhan, Y. Liu, M. Nachtegaal, M. Zebarjadi, J. Arbiol, M. V. Kovalenko and A. Cabot, *Nat. Commun.*, 2016, **7**, 10766.
3 H. J. Van Hook, *Econ. Geol.*, 1960, **55**, 759–788.

4 L. A. Olsen, K. Friese, E. Makovicky, T. Balic-Zunic, W. Morgenroth and A. Grzechnik, *Phys. Chem. Miner.*, 2011, **38**, 1–10.
5 E. Makovicky and D. Topa, *Mineral. Mag.*, 2014, **78**, 387–414.
6 L. A. Olsen, T. Balic-Zunic, E. Makovicky, A. Ullrich and R. Miletich, *Phys. Chem. Miner.*, 2007, **34**, 467–475.
7 L. A. Olsen, T. Balic-Zunic and E. Makovicky, *Inorg. Chem.*, 2008, **47**, 6756–6762.
8 F. Cuccu, L. De Luca, F. Delogu, E. Colacino, N. Solin, R. Mocci and A. Porcheddu, *ChemSusChem*, 2022, **15**, 202200362.
9 R. R. A. Bolt, J. A. Leitch, A. C. Jones, W. Nicholson and D. L. Browne, *Chem. Soc. Rev.*, 2022, **51**, 4243–4260.
10 P. Julien and T. Friscic, *Cryst. Growth Des.*, 2022, **22**, 5726–5754.
11 A. Krusenbaum, S. Grätz, G. T. Tigineh, L. Borchardt and J. G. Kim, *Chem. Soc. Rev.*, 2022, **51**, 2873–2905.
12 X. G. Liu, Y. J. Li, L. Zeng, X. Li, N. Chen, S. B. Bai, H. N. He, Q. Wang and C. H. Zhang, *Adv. Mater.*, 2022, **34**, 2108327.
13 A. A. L. Michalchuk and F. Emmerling, *Angew. Chem., Int. Ed.*, 2022, **61**, e202117270.
14 M. J. Xuan, C. Schumacher, C. Bolm, R. Göstl and A. Herrmann, *Adv. Sci.*, 2022, **9**, 2105497.
15 M. Baláz, L. Tkáciková, M. Stahorsky, M. Casas-Luna, E. Dutková, L. Celko, M. Kovacová, M. Achimovicová and P. Baláz, *ACS Omega*, 2022, **7**, 27164–27171.
16 E. Dutkova, M. Balaz, M. J. Sayagues, J. Kovac and J. Kovac, *Crystals*, 2023, **13**, 487.
17 P. Baláž, E. Dutková, M. Baláž, N. Daneu, L. Findoráková, J. Hejtmánek, P. Levinský, K. Knížek, M. Bali-Hudáková, R. Džunda, R. Bureš and V. Puchý, *Phys. Chem. Chem. Phys.*, 2023, **25**, 31125–31136.
18 P. Baláz, A. B. Burcak, U. Aydemir, A. Mikula, P. Nieroda, M. Baláz, L. Findoráková, R. Bures, V. Puchy, M. Erdemoglu, M. Achimovicová, E. Guilmeau and S. Al Bacha, *Solid State Sci.*, 2024, **151**, 107497.
19 P. Baláz, M. Rajnák, L. Kubicková, M. B. Hudaková, N. Daneu, P. Levinsky, K. Knízek, J. Hejtmánek, J. Navrátil, T. Kmjec, R. Dzunda, M. Achimovicová, O. Sestinová and M. Baláz, *J. Therm. Anal. Calorim.*, 2024, **149**, 10393–10404.
20 Q. W. Zhang and F. Saito, *Adv. Powder Technol.*, 2012, **23**, 523–531.
21 J. H. Li, Q. Tan and J. F. Li, *J. Alloys Compd.*, 2013, **551**, 143–149.
22 J. He and T. M. Tritt, *Science*, 2017, **357**, eaak9997.
23 A. Z. Juhasz and L. Opoczky, *Mechanical Activation of Minerals by Grinding: Pulverizing and Morphology of Particles*, Ellis Horwood, Chichester, 1990.
24 P. Baláž, *Mechanochemistry in Nanoscience and Minerals Engineering*, Springer, Berlin Heidelberg, 2008.
25 R. A. Susilo, Y. Liu, H. W. Sheng, H. L. Dong, R. Sereika, B. Kim, Z. X. Hu, S. J. Li, M. Z. Yuan, C. Petrovic and B. Chen, *J. Mater. Chem. C*, 2022, **10**, 1825–1832.
26 Z. M. Gibbs, H. Kim, H. Wang, R. L. White, F. Drymiotis, M. Kaviany and G. J. Snyder, *Appl. Phys. Lett.*, 2013, **103**, 179902.
27 W. He, Z. X. Wang, T. Zheng, L. Y. Wang and S. W. Zheng, *J. Electron. Mater.*, 2021, **50**, 3856–3861.
28 P. Balaz, E. Dutkova, M. Balaz, R. Dzunda, J. Navratil, K. Knizek, P. Levinsky and J. Hejtmanek, *ChemistryOpen*, 2021, **10**, 806–814.
29 A. M. Callegari and M. Boiocchi, *Mineral. Mag.*, 2009, **73**, 83–94.
30 K. Maji, B. Raveau, S. Fujii, T. Arai, S. Le Tonquesse, C. Prestipino, P. Acharyya, M. Yoshiya and E. Guilmeau, *Chem. Mater.*, 2024, **36**, 4631–4641.
31 W. Liu, B. Chen, L. Xu, D. Wang, C. Xiang, X. Ding and Y. Xiao, *J. Mater. Sci. Technol.*, 2024, **198**, 12–19.
32 M. Ohta, D. Y. Chung, M. Kunii and M. G. Kanatzidis, *J. Mater. Chem. A*, 2014, **2**, 20048–20058.
33 F. G. Cai, R. Dong, W. Sun, X. B. Lei, B. Yu, J. Chen, L. Yuan, C. Wang and Q. Y. Zhang, *Chem. Mater.*, 2021, **33**, 6003–6011.
34 J. Ficeriova, P. Balaz and C. L. Villachica, *Hydrometallurgy*, 2005, **77**, 35–39.
35 H. Rojas-Chávez, G. Carbajal-Franco, H. Cruz-Martínez and J. M. Juárez-García, *Mater. Lett.*, 2024, **370**, 136807.